scientific reports

OPEN

Effect of oxygen vacancy and Si doping on the electrical properties of Ta_2O_5 in memristor characteristics

Md. Sherajul Islam[1,2]✉, Jonghoon Lee[1,3], Sabyasachi Ganguli[1] & Ajit K. Roy[1]✉

The resistive switching behavior in Ta_2O_5 based memristors is largely controlled by the formation and annihilation of conductive filaments (CFs) that are generated by the migration of oxygen vacancies (OVs). To gain a fundamental insight on the switching characteristics, we have systematically investigated the electrical transport properties of two different Ta_2O_5 polymorphs (ϵ-Ta_2O_5 and λ-Ta_2O_5), using density functional theory calculations, and associated vacancy induced electrical conductivity using Boltzmann transport theory. The projected band structure and DOS in a few types of OVs, (two-fold ($O_{2f}V$), three-fold ($O_{3f}V$), interlayer ($O_{IL}V$), and distorted octahedral coordinated vacancies ($O_{\varepsilon}V$)) reveal that the presence of $O_{IL}V$ would cause Ta_2O_5 to transition from a semiconductor to a metal, leading to improved electrical conductivity, whereas the other OV types only create localized mid-gap defect states within the bandgap. On studying the combined effect of OVs and Si-doping, a reduction of the formation energy and creation of defect states near the conduction band edge, is observed in Si-doped Ta_2O_5, and lower energy is found for the OVs near Si atoms, which would be advantageous to the uniformity of CFs produced by OVs. These findings can serve as guidance for further experimental work aimed at enhancing the uniformity and switching properties of resistance switching for Ta_2O_5-based memristors.

Of late, tantalum pentoxide (Ta_2O_5) has been extensively studied for its potential applications in memristors due to its high dielectric constant, high breakdown voltage, and good thermal stability[1–13]. One of the key advantages of Ta_2O_5 as a memristor material is its ability to undergo resistive switching (RS), a phenomenon in which the resistance of the material can be switched between high and low states by applying an electric field. Ta_2O_5 memristors, like other comparable metal oxides, are important due to their potential to revolutionize memory and computing technologies, facilitate new forms of artificial intelligence, curtail energy consumption, and empower the development of intricate and complex systems[8,9,14–17]. Usually, the RS phenomenon in Ta_2O_5 is attributed to the creation and disruption of conductive filaments (CFs) within the material, which can be controlled by the applied voltage and the presence of oxygen vacancies (OVs)[18–20]. However, the formation and characteristics of CFs in Ta_2O_5-based memristors can be complicated and greatly contingent on a number of variables, leading to several challenges in their development and optimization. Attaining consistent and replicable filament formation stands out as a primary obstacle. The formation and stability of CFs may exhibit significant susceptibility to the device configuration, the conditions of deposition, and the materials of the electrode, thereby posing challenges in attaining uniform and foreseeable performance. Hence, optimizing the device fabrication process and materials is crucial for achieving reliable and reproducible filament formation.

Earlier studies demonstrated that OVs are known to act as nucleation sites for the formation of CFs in Ta_2O_5 memristors[18–21]. Besides, OVs affect the stability of the CFs, which in turn can affect the endurance and retention of its resistive states, crucial to memristor's performance reliability. OVs can also affect the switching dynamics of the memristor, including the voltage threshold, switching speed, and noise level. In this context, several studies have investigated the relationship between OVs and the electrical conductivity of Ta_2O_5[22–26]. For example, research has shown that OVs can increase electrical conductivity by creating additional charge carriers and defect states. The concentration and distribution of OVs can also affect the electrical conductivity by altering the material's band structure and carrier mobility. To the best of our understanding, the switching properties

[1]Materials and Manufacturing Directorate, Air Force Research Laboratory, Wright-Patterson Air Force Base, Dayton, OH, USA. [2]Spectral Energies, LLC, Dayton, OH, USA. [3]ARCTOS Technology Solutions, Dayton, OH, USA. ✉email: sheraj_kuet@eee.kuet.ac.bd; ajit.roy@us.af.mil

of Ta_2O_5 based memristor are correlated with the homogeneity of the material's nanoscale CFs. The ability of Ta_2O_5-based memristor to generate CFs may be attributed to the electric field-driven production and spread of OV. However, the existence of many disorders in the deposited resistive layer, the interaction of the OV with the dopant, and the difficulties in accurately defining the RS processes have made progress in this area difficult. To limit material trials and clarify the impact on system operation, it is helpful to have a theoretical knowledge of these defects. Therefore, it is critical to investigate how different dopants affect OV and how Ta_2O_5 -based memristor performance be improved.

On the other hand, depending on the fabrication method and conditions, Ta_2O_5 can exist in different crystal structures such as α-Ta_2O_5, β-Ta_2O_5, and ε-Ta_2O_5 phases[27–39] that can affect the performance of the memristor. The most commonly used structure of Ta_2O_5 is the amorphous phase[40]. This is because amorphous Ta_2O_5 can undergo a reversible RS phenomenon that is essential for the operation of memristors. Other structures of Ta_2O_5, such as the orthorhombic, tetragonal, monoclinic, and cubic phases, may also be used for memristor applications[32,34,37]. However, these structures may require additional processing steps, such as annealing or doping, to achieve the desired properties for memristor operation. Moreover, a hidden polymorph namely called as lambda phase (λ-Ta_2O_5) can also exist[30]. Different crystal structures of Ta_2O_5 may exhibit different resistive switching behaviors because the breakdown voltage should be different for each structure (usually proportional to the square of the bandgap energy), which can make it challenging to optimize the performance of the device. To fully understand the switching mechanism of Ta_2O_5 in memristors, it is important to identify the mechanisms involved in the switching behavior, such as materials crystalline phase influencing oxygen migration and defect formation, and to understand how these mechanisms are affected by different experimental conditions stated above.

In this work, instead of studying all Ta_2O_5 crystalline phases we discussed above, we limit our work investigating the vacancy induced electrical transport properties of orthorhombic and lambda phase Ta_2O_5, due to their good agreement with the experimentally observed electrical band gap of amorphous Ta_2O_5, using density functional theory investigations. The effect of OV on the electrical conductivity of Ta_2O_5 has been calculated using Boltzmann transport theory. Chemical doping, combined with OVs, is known in many cases to impact the performance of Ta_2O_5 memristors and help optimize key parameters such as the RS characteristics, endurance, retention, and variability. Although several molecules as dopant to Ta_2O_5 are feasible[41–43], however, here only the combined effect of Si-doping and OV on electrical conductivity are investigated. To explore the local structural changes due to OV and doping effect, the formation energy, projected electronic band structure, and projected density of states have been calculated. This study can guide further experimental efforts aimed at enhancing the uniformity of RS and switching properties of Ta_2O_5-based memristor devices.

Calculation methods

All the investigations have been conducted using the ab initio first-principles plane wave pseudopotential approach executed in the Vienna Ab initio Simulation Package (VASP)[44,45]. The electron exchange correlation is obtained using the generalized gradient approximation of the Perdew-Burke-Ernzerhof solid (GGA-PBEsol) functional[46]. The structure is optimized using the RMM-DIIS algorithm with the force convergence of 0.02 eV/Å (1×10^{-5} eV). Following relaxation, the electronic structures are characterized using a kinetic energy cutoff of 400 eV. The Brillouin-zone is sampled with a k-point mesh of $17 \times 13 \times 9$ for the structural relaxations and all the electronic properties calculations. The electrical conductivity has been calculated using the Boltzmann transport theory as implemented in MedeA VASP. Using the Boltzmann transport theory[47], one can represent the electrical conductivity tensor of a solid in terms of energy dependence as

$$\sigma_{\alpha\beta}(E) = \frac{e^2}{\Omega_C}\sum_k\sum_n\left(-\frac{\partial f(E)}{\partial E}\right)v_{kn}^{\alpha}v_{kn}^{\beta}\tau_{kn} \tag{1}$$

where *f*(E) denotes the Fermi function $f(E) = \frac{1}{e^{\beta(E-\mu)}+1}$, with μ being the chemical potential, $\beta = \frac{1}{k_BT}$. τ_{kn} stands for the relaxation time, which relies on the band index (n), spin, and k-point and replicates phenomena such as electron–phonon scattering on the electronic states. v_{kn}^{α} represents the group velocity. The first derivative of the band energy (ϵ_{kn}) with respect to the appropriate Cartesian component (α) of the k-vector yields the v_{kn}^{α} for each band (n) and k-point as

$$v_{kn}^{\alpha} = \frac{1}{\hbar}\frac{\partial\epsilon_{kn}}{\partial k_{\alpha}} \tag{2}$$

The electrical conductivity can further be reduced by relating the so-called transport distribution[47,48] as

$$\Xi_{\alpha\beta}(E) = \frac{1}{\Omega_C}\sum_k\sum_n v_{kn}^{\alpha}v_{kn}^{\beta}\tau_{kn}\delta(E-\epsilon_{kn}) \tag{3}$$

Thus, the electrical conductivity coefficient, $\sigma_{\alpha\beta}$ can be represented as

$$\sigma_{\alpha\beta} = e^2\int_{-\infty}^{\infty}dE\left(-\frac{\partial f(E)}{\partial E}\right)\Xi_{\alpha\beta}(E) \tag{4}$$

To calculate electrical conductivity, the self-consistent field (SCF) charge density of the complete system is determined in the first stage with a k-point mesh of $9 \times 5 \times 5$. Based on the SCF charge density obtained in the preceding phase, the Fermi surface and a band structure are then generated with a relatively fine and regular

k-point grids of 17 × 13 × 9. The band structure acquired in the second phase is then used to compute the electronic transport characteristics using the BoltzTraP code[49].

Results and discussion

Among many different polymorphs of Ta_2O_5 that have been discovered, the β-Ta_2O_5 (orthorhombic space group P*mmm*)[35,39,50–53] is the most studied polymorph because it is thought to be stable at low temperatures and experience a phase transition to α-Ta_2O_5 at relatively high temperatures (1630 K)[39]. Another common phase is ϵ-Ta_2O_5 (space group C2/c)[36], which can be produced using either a chemical method[36] or a high-pressure synthesis[37]. The amorphous phase, the hexagonal or δ phase, the high-pressure-prepared phase, and the polymorph with a high number of OVs can also be detected by the X-ray particle diffraction observations[31–33,54]. In addition, λ-Ta_2O_5 has drawn a lot of attention recently due to its high structural stability and good agreement with the experimentally observed electrical band gap of amorphous Ta_2O_5[30]. We primarily concentrate on the last two demonstrative phases, specifically ϵ-Ta_2O_5[37,55–58] and λ-Ta_2O_5[19,59,60], as they can be produced under comparatively favorable circumstances and are generally thought to be sufficiently stable for use in real-world applications, as compared to the other phases. It is noted that our examination of various Ta_2O_5 polymorphic structures is by no means comprehensive; instead, the primary focus of this article is on analyzing the impacts of varying OVs on certain electronic transport characteristics. ϵ-Ta_2O_5 phase belongs to the monoclinic structure with the C2/c symmetry and λ-Ta_2O_5 phase belongs to the orthorhombic structure with the Pbam symmetry. In ϵ-Ta_2O_5 crystal structure, each Ta atom has a distorted octahedral coordination environment, with six neighboring O atoms. On the other hand, three different O sites can be found in the λ-Ta_2O_5 structure: the doubly and threefold coordinated sites in the Ta_2O_3 plane, as well as the twofold coordinated site of the Ta-O-Ta interlayer chain, as shown in Fig. 1. The calculated lattice parameters of the optimized structures of both phases along with the experimentally obtained values are presented in Table 1. The optimized lattice parameters derived from PBEsol computations for both λ-Ta_2O_5 and ϵ-Ta_2O_5 structures show excellent agreement with experiment and theoretical predictions (left column in Table 1)[30,37], which also indicating that the PBEsol GGA functional performs well in forecasting structural characteristics of solid. In light of this, the PBEsol optimized structure could be used as a suitable beginning point for the ensuing electronic structure computations. The analyses start with the calculations of different types of OVs-induced electrical conductivity for two different phases of Ta_2O_5. In λ-Ta_2O_5 structure, three types of OVs are defined according to their coordination sites such as O_{2f}V, O_{3f}V, and O_{IL}V. The OV in ϵ-Ta_2O_5 structure is represented by the OϵV. We have taken 2 × 2 × 1 and 2 × 1 × 1 supercells for λ-Ta_2O_5 and ϵ-Ta_2O_5 structures, respectively, which contains 16 Ta atoms and 40 O atoms for both structures. The estimated electrical conductivity for different types of OVs is shown in Fig. 2.

The calculated results revealed that with the introduction of a single OV, the electrical conductivity tends to increase for all types of vacancy defects, although the increase of conductivity for all the vacancy types is not the same. OϵV, O_{2f}V, and O_{3f}V type vacancy defects show a slight increase in conductivity compared to the pristine Ta_2O_5. In contrast, the O_{IL}V defect shows a considerable increase in conductivity. In general, OVs can act as

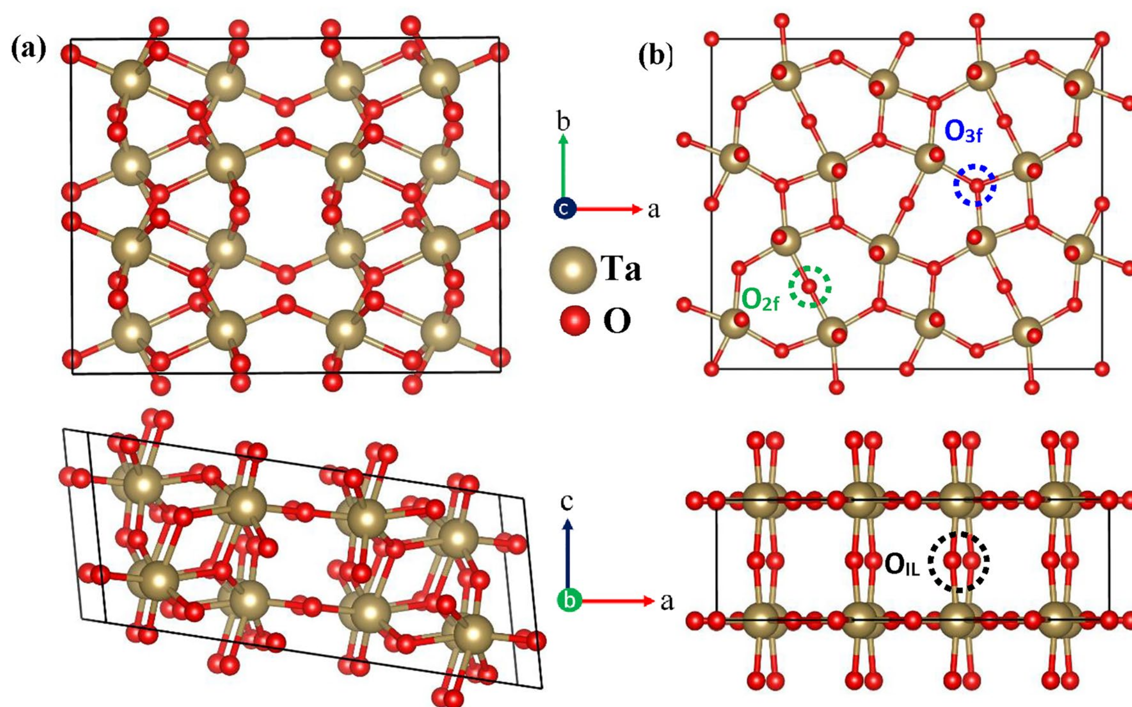

Figure 1. Structural model for (**a**) ϵ-Ta_2O_5 and (**b**) λ-Ta_2O_5 phases. Upper and lower figures indicate the 'ab' and 'ac' plane views of ϵ-Ta_2O_5 and λ-Ta_2O_5 structures, respectively. Green, blue, and black circles in (**b**) indicate twofold, threefold, and interlayer coordinated O atoms, which are denoted as O_{2f}, O_{3f}, and O_{IL}, respectively.

Chemical formula	ϵ-Ta_2O_5[37]	This work	λ-Ta_2O_5[30]	This work
Cell setting	Monoclinic	Monoclinic	Orthorhombic	Orthorhombic
Space group	C2/c	C2/c	Pbam	Pbam
a (Å)	12.7853	12.74156	6.25	6.216
b (Å)	4.8537	4.8200	7.40	7.338
c (Å)	5.5276	5.49353	3.83	3.798
α (°)	90	90	90	90.00
β (°)	90	90	90	90.00
γ (°)	104.264	104.22	90	90.00

Table 1. Calculated structural parameters of ϵ-Ta_2O_5 and λ-Ta_2O_5 phase.

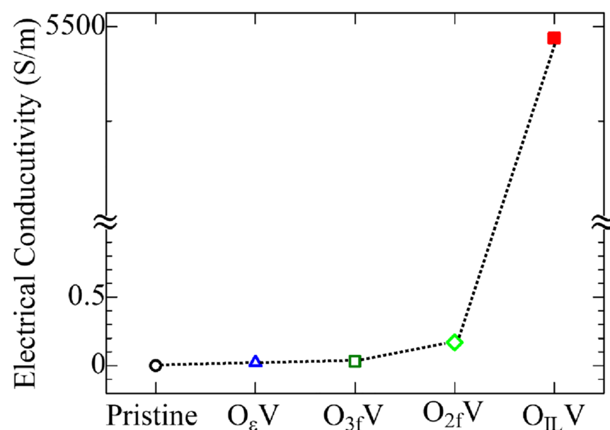

Figure 2. Electrical conductivity of different types of oxygen vacancies induced Ta_2O_5 at room temperature (300 K).

electron traps, leading to changes in the electronic structure of the material and altering its electrical conductivity. In the case of Ta_2O_5, OVs are expected to enhance the electrical conductivity of the material because the presence of OVs introduces electronic states within the band gap of Ta_2O_5, which can act as charge carriers and increase the conductivity. These electronic states are usually located closer to the conduction band, which means that electrons can easily move into these states and contribute positively to the conductivity. Experimental studies have confirmed that oxygen vacancies do indeed affect the electrical conductivity of Ta_2O_5. For example, Seki et al. found that annealing Ta_2O_5 films in reducing atmospheres (i.e., environments with a low oxygen partial pressure) resulted in a significant increase in the films' electrical conductivity[61]. This was attributed to the creation of OVs in the material.

To comprehend the vacancy induced electrical conductivity in both structures, we have calculated the electronic band structure for all these types of vacancies. The electronic band structure from PBEsol for pristine ϵ -Ta_2O_5 and λ-Ta_2O_5 structures are presented in supplementary information (Figure S1). The ϵ-Ta_2O_5 structure shows a larger band gap by pushing the conduction band minimum (CBM) to higher energy compared to the λ-Ta_2O_5 structure. An electronic gap of 3.18 eV and 2.16 eV is observed for ϵ-Ta_2O_5 and λ-Ta_2O_5 structures, respectively. The obtained bandgap is well matched with the previous studies[19,30,37]. It is worth to mention, earlier investigations demonstrated that HSE functional may estimate a higher band gap compared to PBE functional[19,30]. However, our focus here is to understand how conductivity is changed due to OVs, and hence the PBEsol is justifiably an acceptable choice for this study. It is evident from the band structures that the O atoms form the valence bands, while the conduction bands are formed by the delocalized electrons of the Ta atoms, as shown in Fig. 3. As evident from the data in Fig. 3, the OVs in Ta_2O_5 can reduce the band gap of the material through the formation of defect states within the band gap. When an O atom is missing from the crystal lattice, there is a local change in the charge balance within the crystal, leading to the formation of electronic defect states. This defect state can act as an intermediate energy level between the valence and conduction bands, allowing electrons to be promoted across the bandgap more easily. This may cause an increase in the conductivity of the materials. However, the energy gap between the CBM and the defect band energy (DBE) is ~ 0.8 eV, and between the valence band maximum (VBM) and the DBE is ~ 2 eV (as shown in Fig. 3a–c). Both gaps are too large for the electron transition at room temperature (25 meV). The degree to which the bandgap is affected by OVs in Ta_2O_5 depends on the types of vacancies within the material.

Removing one O atom from $O\epsilon$, O_{2f}, and $O_{3f.}$ coordinated sites do not occupy vacant conduction band states to render the system metallic; rather they confine in a mid-gap defect state, confined at the vacancy site as shown

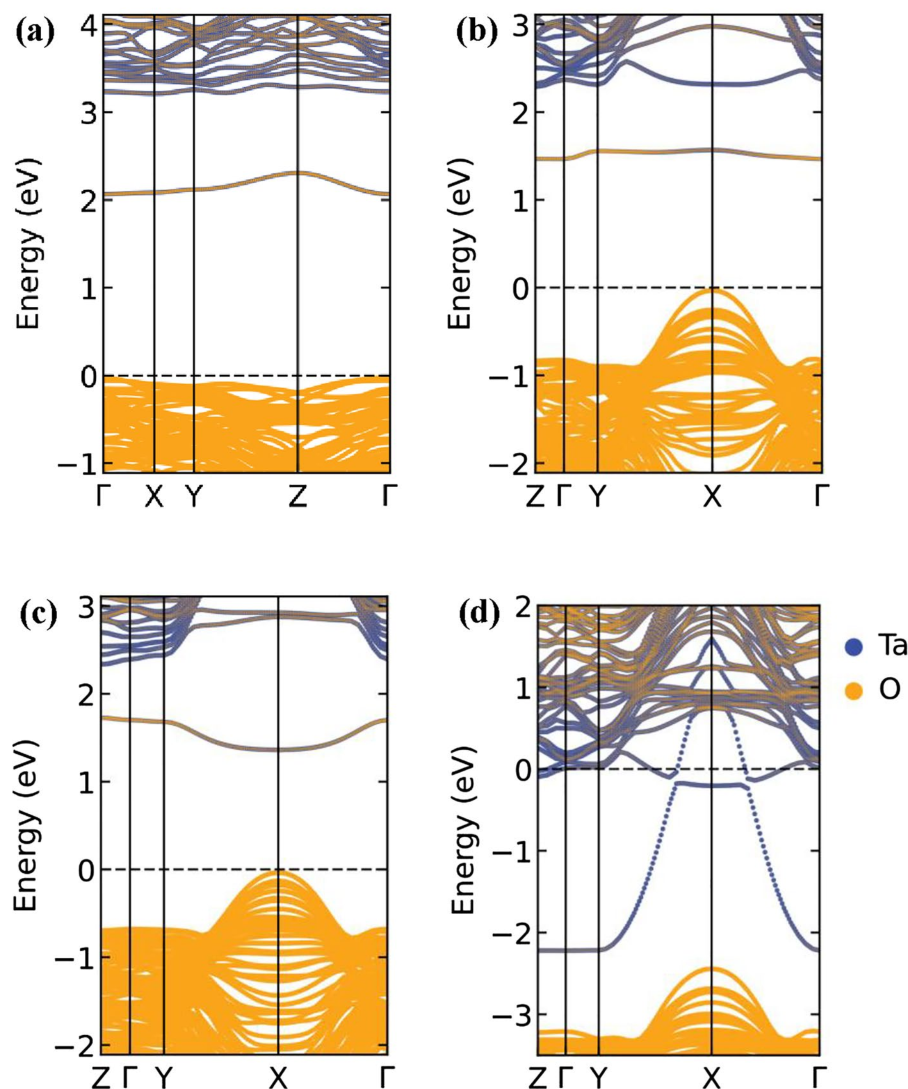

Figure 3. Projected electronic band structures of Ta_2O_5 with single (**a**) OϵV in ϵ-phase, and (**b**) $O_{2f}V$, (**c**) $O_{3f}V$, and (**d**) $O_{IL}V$ type defects in λ-phase. The reference energy level (dotted line) is touched with the valence band maximum for all types of OVs. Yellow and blue colors represent the contribution form O and Ta atoms, respectively.

Fig. 3a–c. The defect states just lead to the appearance of additional electronic states within the bandgap, without necessarily changing the overall band structure of the material. The system is semiconducting in all instances because there is a gap between the highest occupied and lowest unoccupied states. The estimated energy differences between the conduction band and the defect states are 0.877 eV, 0.606 eV and 0.614 eV for OϵV, $O_{2f}V$, and $O_{3f}V$ type vacancy defects, respectively. On the other hand, the introduction of the $O_{IL}V$ defect results in a semiconductor-to-metal transition. The semiconductor to metal transition due to an $O_{IL}V$ type defect is characterized by the filling of the conduction band with electrons, resulting in a partially filled conduction band that is characteristic of metals, as shown in Fig. 3d. This leads to higher electrical conductivity for this type of vacancies. It is worth noting that the effects of OVs on the bandgap of Ta_2O_5 are complex and can be influenced by a variety of factors, including the crystal structure of the material, the nature of the OVs themselves, and the presence of other impurities or defects in the material. Therefore, a thorough understanding of the properties of Ta_2O_5 and its behavior in different environments is necessary to accurately predict and control its bandgap energy.

We have thus further assessed the projected density of states (PDOS) to get more information on the nature of the electronic transitions that occur in the material and the role of OV defects and impurities in the electronic structure. Figure 4 shows the PDOS for various types of OV defects for both λ-Ta_2O_5 and ϵ-Ta_2O_5 phases, respectively. The presence of OVs in Ta_2O_5 significantly affect its PDOS due to the changes in the electronic structure caused by the introduction of defect states. It is observed from PDOS that the valence band is mainly composed of oxygen p-orbitals and the conduction band is mainly composed of Ta d-orbitals. The PDOS of Ta_2O_5 without any OVs typically shows a band gap between the valence band and the conduction band, as shown in supplementary information (Figure S2). When OVs are introduced into the Ta_2O_5 lattice, the electronic structure

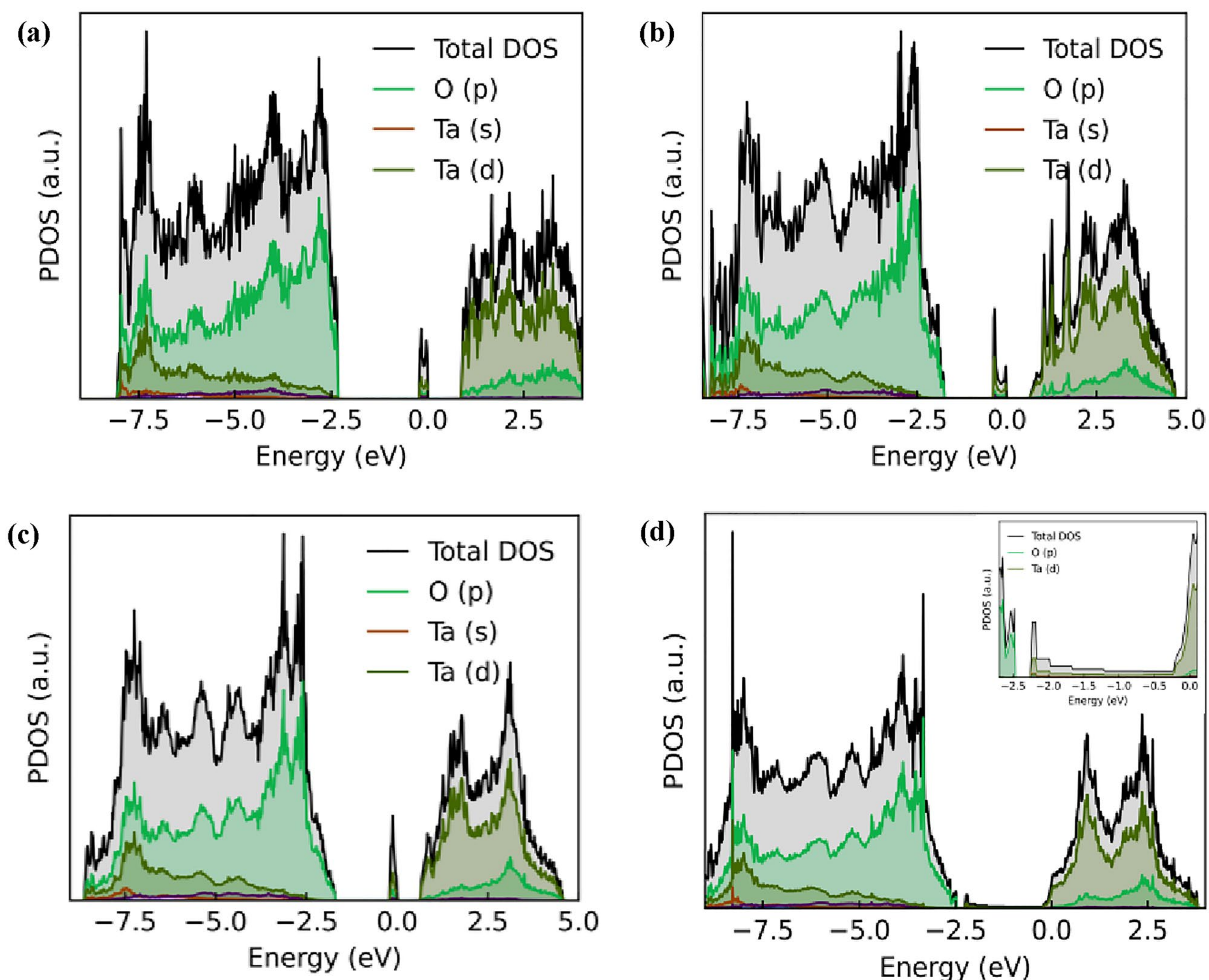

Figure 4. PDOS of Ta_2O_5 with single (**a**) OϵV, (**b**) O_{2f}V, (**c**) O_{3f}V, and (**d**) O_{IL}V type defects. Inset shows the zoom-in view of a broadened peak covering the entire gap region.

changes due to the formation of defect states within the band gap. OVs lead to the appearance of new peaks and features in the PDOS of both λ-Ta_2O_5 and ϵ-Ta_2O_5 structures. In terms of specific PDOS contributions, the OVs in Ta_2O_5 can lead to an increase in the density of states near the Fermi level associated with the Ta 5d orbitals and the O 2p orbitals. This indicates that the electronic states associated with these orbitals are more strongly affected by the OVs.

The number and position of the defect states depend on the location of the oxygen vacancies in the lattice. Although some sharp peaks are observed in the middle of the gap for OϵV, O_{2f}V and O_{3f}V defects, a broadened peak covers the entire gap region for O_{IL}V type defect, indicating the semiconductor to metal transition in this defect type. Moreover, it is observed that the Fermi level is shifted towards the conduction band with the introduction of OV. The Fermi level for semiconductor (insulator) at 0 K is simply at (VBM + CBM)/2. In Fig. 3a–c, the Fermi level should be at (CBM + DBE)/2 at 0 K because the highest occupied state is at the top of DBE, indicating that the Fermi level moves towards the conduction band for all types of OVs. The OV causes the Fermi level to move; therefore, the distribution f(E) in Eq. 4 changes with the OV. The integral sampling over E in Eq. 4 has the heavier weight of f(E) when E is near the Fermi level. Now, with OV, the Fermi level moved closer to the conduction band, which increased the weight f(E) for the conduction band. Furthermore, the Fermi level lies in the middle between DBE and CBM at 0 K, which further moves closer to CBM as temperature increases. The DFT calculated values of Fermi energy for λ and ϵ-phase pristine structures are 2.17 eV and 2.008 eV, respectively, whereas these values are 4.351 eV, 3.805 eV, 3.856 eV, and 4.5009 eV for OϵV, O_{2f}V, O_{3f}V and O_{IL}V type defects, respectively, as shown in Fig. 5. The shifting of Fermi energy towards the conduction band leads to an increase in the number of free electrons available for conduction, which can increase the electrical conductivity of the material. When OVs are present, the oxygen 2p states near the CBM become empty, and some of the electrons from the Ta 5d states may transfer to these vacant oxygen states. This transfer of electrons leads to an increase in the Fermi energy level and a shift towards the CBM. The increase in electrical conductivity due to a Fermi level shift towards the conduction band is observed in many types of materials, including semiconductors, metals, and insulators[62–66].

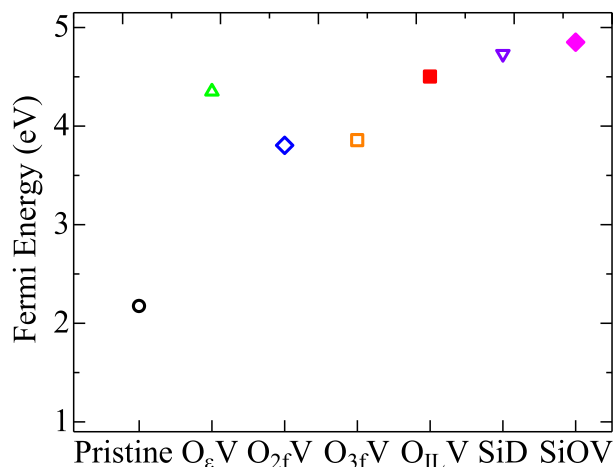

Figure 5. Changes of Fermi energy for different types of oxygen vacancies.

We have also estimated the formation energy (E_{fe}) for each of the aforementioned defect types. The E_{fe} of OVs in Ta_2O_5 is closely associated to the SET/RESET voltage and power utilization of the memristor during RS[19], as it represents the defect-forming capability and the stability of defects. The voltage needed to move the device from a high-resistance state (HRS) to a low-resistance state (LRS) is known as the SET voltage, whereas the voltage needed to transfer the device from a LRS to a HRS is known as the RESET voltage. If the E_{fe} of OVs is too low, it can result in a high concentration of vacancies, which can lead to poor endurance and retention characteristics. Therefore, it is important to optimize the E_{fe} of OVs in Ta_2O_5-based memristors to achieve the desired SET/RESET voltage and power consumption while maintaining good endurance and retention characteristics. This can be achieved by tuning the material composition, crystal structure, and processing conditions to control the concentration and distribution of defects in the material. The E_{fe} of OV can be evaluated using the expression[67–70] as, $E_{fe} = E_{OV} - E_{pristine} - \sum n\varsigma$, where E_{OV} and $E_{pristine}$ represent the total energy of the OV-defected and pristine structures, respectively. The number of atoms necessary to create OV is n. If n is greater than 0 then it is necessary to add atoms to the defect-free model, and if n is less than 0 then it is necessary to delete atoms from the pristine model. ς stands for the chemical potential of the associated atom. The value of ς for the oxygen atom is used in the calculation as 4.93 eV[19]. The calculated E_{fe} for the OϵV, O_{2f}V, O_{3f}V, and O_{IL}V are 6.50 eV, 6.21 eV, 5.25 eV, and 4.40 eV, respectively, which is relatively high. However, this finding is in line with the earlier investigations[71]. Among the E_{fe} calculated for all OV types, the O_{IL}V shows the comparatively lowest value, indicating that this type of OV is more likely to be present in the system. While the generation and manipulation of specific types of OVs pose challenges, various processes can be employed to achieve this, including oxygen annealing or sputtering in controlled atmospheres during device fabrication, electroforming through the application of high-voltage pulses or voltage sweeps across the memristor, and the utilization of voltage or temperature variations.

Finally, in search for lowering the high SET/REST voltage predicted above, we have investigated the doping effect and explored the combined doping and OV effect on the electrical properties in Ta_2O_5. To investigate the doping effect, we have considered ϵ-Ta_2O_5 structure as a representational unit as its electrical properties are closer to the realistic applications. It is revealed that the doping of N atom in Ta_2O_5 structure decreases the band gap and follows the sequence of oxide > oxynitride > nitride, which is in good agreement with experimental results as well[58]. It is worthy to note that several studies have been performed in improving the electronic properties of Ta_2O_5-based resistive memristor devices using ionic doping technology. Some successful doping strategies include Ti doping[41], which has been shown to produce soft collapse with high ON/OFF ratio in Ta_2O_5-RRAM devices. Al doping has also been found to reduce the forming voltage required for the device to switch states[42]. More recently, Zr doping has been shown to produce better switching performance in Ta_2O_5-RRAM[43]. However, it is important to note that metal dopants can also have negative effects on device performance. For example, metal dopants can cause field enhancement effects that would reduce the stability and uniformity of CFs produced by OVs as the number of cycle increases[72,73]. This can lead to deterioration in the high resistive state retention of the device, which can limit its overall performance and reliability. In contrast, the use of nonmetallic Si dopants in Ta_2O_5-RRAM devices may offer a promising approach for improving the performance and reliability of these devices, particularly in terms of maintaining uniform CFs and avoiding the negative effects of field enhancement[19]. We have thus replaced one O atom with one Si atom in ϵ-Ta_2O_5 structure and then OVs are created by removing O atoms. The OV-induced projected band structure and projected density of states of Si-doped ϵ-Ta_2O_5 are represented in Fig. 6. An earlier study revealed that the OV in Si-doped Ta_2O_5 may have negligible effect on conductivity as there is no defect state in the band gap and the defect energy level is close to the VBM[19]. However, our calculated projected band structures and PDOS clearly state that the introduction of OVs in Si-doped Ta_2O_5 leads to the formation of defect states near the conduction band edge, which can participate in electronic transport. There are possibly two factors contributing to the different simulation outcomes seen in the earlier study conducted by Cai et al.[19] It should firstly be noted that the positioning of the Si element

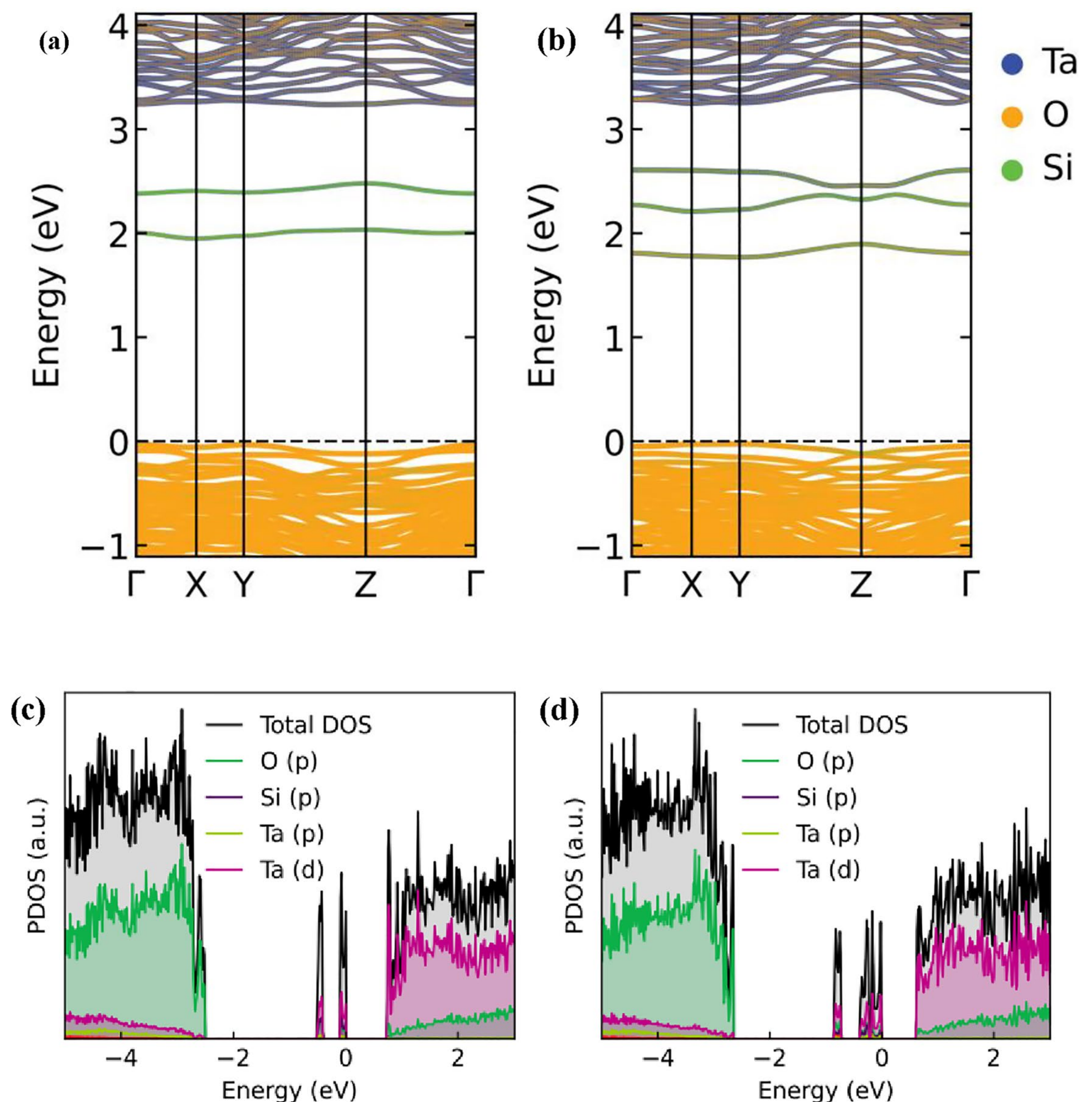

Figure 6. Projected electronic band structure of ϵ-Ta_2O_5 structure with (**a**) Si-doping and (**b**) combined Si-doping and one OV. PDOS of ϵ-Ta_2O_5 structure with (**c**) Si-doping and (**d**) combined Si-doping and one OV.

is not the same. In the aforementioned work, the Ta atom was replaced with a Si dopant, but in the current investigation, the O atom is replaced by the Si dopant. Furthermore, the study conducted by the Cai et al. focused on the λ-Ta_2O_5 phase, while our current research investigates the Si-doped features inside the ϵ-Ta_2O_5 structure. Several experimental[55,74] and theoretical investigations[58,75–77] have shown that the substitution of the O atom in ϵ-Ta_2O_5 with a N dopant may lead to significant alterations in its electrical and optical characteristics. Based on the findings of prior experimental and theoretical investigations, we have chosen to examine the impact of doping by replacing O atoms with Si in the ϵ-Ta_2O_5 structure. When investigating the RS of Ta_2O_5-based memristor, it is important to consider the E_{fe} of OVs, the conductivity of the Ta_2O_5 layer, and the interaction of dopants with OV, as these factors can affect the stability and regularity of CFs in the device[78,79]. The calculated energy gaps between defect state and conduction band of Si-doped and combined Si-doped with OV are 0.73 eV, 0.584 eV, respectively. As can be seen in Fig. 6, with the creation of OV in Si-doped Ta_2O_5, the PDOS shows broadened and increased peaks in the vicinity of the Fermi level, indicating the presence of defect states that can increase the conductivity of the material.

Additionally, the Fermi energy increases and shifts towards the conduction band, which further enhances the conductivity. Furthermore, it is observed that the calculated formation energy for single OϵV in Si-doped ϵ-Ta_2O_5 reduces to a lower value of 4.12 eV, which may cause the reduction in SET/RESET voltage in Si-doped Ta_2O_5-based memristor[80]. The presence of the silicon dopant should also have a stabilizing effect providing consistency on the OVs in the vicinity of those O atoms. To check this, we have analyzed the E_{fe} of OVs at different positions of Si doped Ta_2O_5. The O atoms at three locations are removed and corresponding E_{fe} are calculated, as shown in Fig. 7. The obtained formation energies are 4.12 eV, 5.05 eV, and 5.78 eV for the three

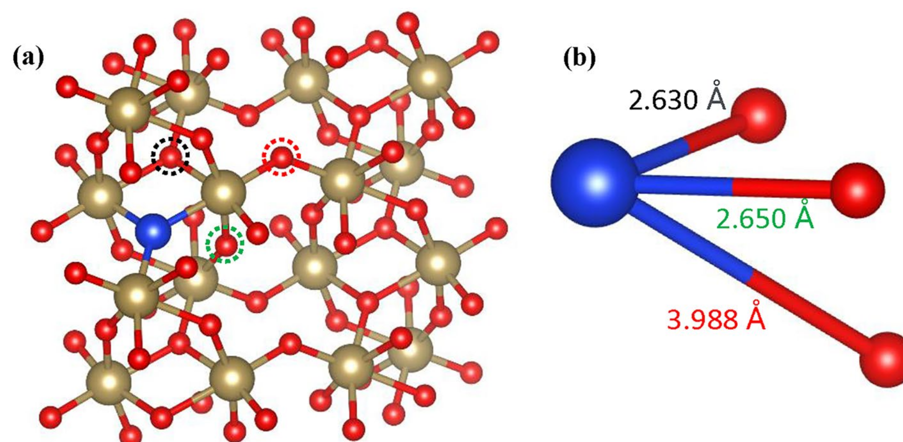

Figure 7. (**a**) Si-doped ϵ-Ta_2O_5 structure combined with oxygen vacancies. Different colors in the dotted circles represent different positions of the O atom with respect to the Si atom. The blue, tan, and red spheres denote the Si, Ta, and O atoms, respectively. (**b**) Distances of O atom from Si atom for different sites.

different distances of 2.630 Å, 2.650 Å, and 3.988 Å, respectively. We observed that the O atoms located near to the Si impurity have a comparatively low E_{fe} of OVs. These findings fit the previous research well[19]. This is likely due to the influence of the Si dopant on the electronic structure and bonding environment of the neighboring oxygen atoms. We have calculated the interaction energy, $E_{interaction}$ between the Si dopant and OV using the relation as $E_{interaction} = E_{SiOV} - E_{separate}$. Here, E_{SiOV} denotes the energy of the combined Si-doping and OV and $E_{separate}$ denotes the energy of the separate defect generated by the Si atom and OV. Our calculation showed that the interaction energy between the Si atom and OV is ~ 2.20 eV, demonstrating a significant attraction between OV and Si atom. Hence, OV develops in the vicinity of the Si atom, which is advantageous to the uniformity of CFs produced by OVs. This phenomenon is in line with the capacity of the Si dopant to impede the stochastic generation of CFs triggered by OVs[19]. The DFT simulations present here provide insight into performance trends, which is valuable in assisting in material selection and optimization for improved switching, guiding experimental efforts.

The determination of the doping characteristics of a defect relies heavily on the computation of the charge state of the point defect. Nevertheless, we believe that the issue of the OV charge state in memristors is more complex than the typical formation energy and transition level calculations for the single-point defect, which are often carried out for dopant analysis. The most stable charge state of OV should vary with the local environment because the formation energy of charged defects is a function of Fermi level, whereas that of neutral defects is not. We may determine the charge state of OV assuming an isolated single defect. Then, the initial charge state of OV calculated shall dictate the transport of single OV under external electrical bias. Nevertheless, the charge state of OV may change further during the course as the local concentration of OV varies along with Fermi level to form a filament where the OV charge state should return to neutral. Due to the greater complexity of the function of OV in memristors compared to dopants in semiconductors, we posit that a distinct examination of the charge state of OV in memristor applications is merited.

Conclusions

In conclusions, the electrical transport characteristics of ϵ-Ta_2O_5 and λ-Ta_2O_5 polymorphs have been thoroughly examined using density functional theory calculations. Boltzmann transport theory is used to determine the vacancy-induced electrical conductivity of both structures. Creation of vacancy defects in Oϵ, O_{2f}, and O_{3f} coordinated sites generate localized mid-gap defect states within the energy bandgaps. In contrast, the introduction of the $O_{IL}V$ defect results in a semiconductor-to-metal transition in Ta_2O_5, leading to an improved electrical conductivity. The $O_{IL}V$ also shows the lowest formation energy, indicating the lower voltage required for SET/RESET process for this type of vacancy. The introduction of OVs leads to a shift in the Fermi level towards the conduction band for all types of OVs, which can aid in electronic transport and boost conductivity. Further, the formation energy is found to be lowered in Si-doped Ta_2O_5, which depends on the OV location, with the lowest energy found for the OV located closest to the Si atom- this appears to be advantageous to the uniformity of CFs produced by OVs. These results can act as guidelines for additional experimental work aimed at improving the regularity and switching characteristics of RS for Ta_2O_5-based resistive random-access memory.

Data availability

The datasets used and/or analyzed during the current study available from the corresponding author on reasonable request.

Received: 12 July 2023; Accepted: 29 September 2023
Published online: 03 October 2023

References

1. Kao, C.-H., Chen, H., Chiu, J. S., Chen, K. S. & Pan, Y. T. Physical and electrical characteristics of the high-k Ta_2O_5 (tantalum pentoxide) dielectric deposited on the polycrystalline silicon. *Appl. Phys. Lett.* **96**, 112901 (2010).
2. Breuer, T. *et al.* Realization of minimum and maximum gate function in Ta_2O_5-based memristive devices. *Sci. Rep.* **6**, 23967 (2016).
3. Shyam, B. *et al.* Measurement and modeling of short and medium range order in amorphous Ta_2O_5 thin films. *Sci. Rep.* **6**, 32170 (2016).
4. Lee, A. R. *et al.* Memory window engineering of Ta_2O_5–x oxide-based resistive switches via incorporation of various insulating frames. *Sci. Rep.* **6**, 30333 (2016).
5. Park, T. H. *et al.* Thickness effect of ultra-thin Ta_2O_5 resistance switching layer in 28 nm-diameter memory cell. *Sci. Rep.* **5**, 15965 (2015).
6. Kim, T. *et al.* Reversible switching mode change in Ta_2O_5-based resistive switching memory (ReRAM). *Sci. Rep.* **10**, 11247 (2020).
7. Yan, X. *et al.* Memristors based on multilayer graphene electrodes for implementing a low-power neuromorphic electronic synapse. *J. Mater. Chem. C* **8**, 4926–4933 (2020).
8. Hu, W., Zou, L., Gao, C., Guo, Y. & Bao, D. High speed and multi-level resistive switching capability of Ta_2O_5 thin films for non-volatile memory application. *J. Alloys Compd.* **676**, 356–360 (2016).
9. Wang, J. *et al.* A radiation-hardening Ta/Ta_2O_5-x/Al_2O_3/$InGaZnO_4$ memristor for harsh electronics. *Appl. Phys. Lett.* **113**, 122907 (2018).
10. Yan, X. *et al.* Artificial electronic synapse characteristics of a Ta/Ta_2O_5-x/Al_2O_3/$InGaZnO_4$ memristor device on flexible stainless steel substrate. *Appl. Phys. Lett.* **113**, 013503 (2018).
11. Jagath, A. L., Kumar, T. N. & Almurib, H. A. F. Electrical model of Ta_2O_5/TaOx RRAM device with current conduction beyond RESET phase. In *2019 IEEE 9th International Nanoelectronics Conferences (INEC)* 1–5 (2019). https://doi.org/10.1109/INEC.2019.8853845.
12. Wang, W. *et al.* Tantalum pentoxide (Ta_2O_5 and Ta_2O_5-x)-based memristor for photonic in-memory computing application. *Nano Energy* **106**, 108072 (2023).
13. Lee, T. S. & Choi, C. Improved analog switching characteristics of Ta_2O_5-based memristor using indium tin oxide buffer layer for neuromorphic computing. *Nanotechnology* **33**, 245202 (2022).
14. Qu, B. *et al.* Synaptic plasticity and learning behavior in transparent tungsten oxide-based memristors. *Mater. Des.* **129**, 173–179 (2017).
15. Min, J.-G., Park, H. & Cho, W.-J. Milk–Ta_2O_5 hybrid memristors with crossbar array structure for bio-organic neuromorphic chip applications. *Nanomaterials* **12**, 2978 (2022).
16. Zhang, Y., Shen, Y., Wang, X. & Cao, L. A novel design for memristor-based logic switch and crossbar circuits. *IEEE Trans. Circuits Syst. Regul. Pap.* **62**, 1402–1411 (2015).
17. Lee, M.-J. *et al.* A fast, high-endurance and scalable non-volatile memory device made from asymmetric Ta_2O_5–x/TaO_2–x bilayer structures. *Nat. Mater.* **10**, 625–630 (2011).
18. Prakash, A., Jana, D. & Maikap, S. TaOx-based resistive switching memories: prospective and challenges. *Nanoscale Res. Lett.* **8**, 418 (2013).
19. Cai, C. *et al.* Oxygen vacancy formation and uniformity of conductive filaments in Si-doped Ta_2O_5 RRAM. *Appl. Surf. Sci.* **560**, 149960 (2021).
20. Zahoor, F., Azni Zulkifli, T. Z. & Khanday, F. A. Resistive random access memory (RRAM): an overview of materials, switching mechanism, performance, multilevel cell (MLC) storage, modeling, and applications. *Nanoscale Res. Lett.* **15**, 90 (2020).
21. Wang, C. *et al.* Conduction mechanisms, dynamics and stability in ReRAMs. *Microelectron. Eng.* **187–188**, 121–133 (2018).
22. Balachandran, U. & Eror, N. G. Electrical conductivity in Ta_2O_5. *Mater. Res. Bull.* **17**, 151–160 (1982).
23. Lü, X. *et al.* Pressure-induced amorphization in single-crystal Ta_2O_5 nanowires: A kinetic mechanism and improved electrical conductivity. *J. Am. Chem. Soc.* **135**, 13947–13953 (2013).
24. Sawada, H. & Kawakami, K. Electronic structure of oxygen vacancy in Ta_2O_5. *J. Appl. Phys.* **86**, 956–959 (1999).
25. Lee, J., Lu, W. D. & Kioupakis, E. Electronic and optical properties of oxygen vacancies in amorphous Ta_2O_5 from first principles. *Nanoscale* **9**, 1120–1127 (2017).
26. Tsai, K.-C., Wu, W.-F., Chao, C.-G. & Wu, C.-C. Improving electrical characteristics of Ta/Ta_2O_5/Ta capacitors using low-temperature inductively coupled N_2O plasma annealing. *J. Electrochem. Soc.* **154**, H512 (2007).
27. Hummel, H.-U., Fackler, R. & Remmert, P. Tantaloxide durch Gasphasenhydrolyse, Druckhydrolyse und Transportreaktion aus 2H-TaS2: Synthesen von TT-Ta2O5 und T-Ta2O5 und Kristallstruktur von T-Ta2O5. *Chem. Ber.* **125**, 551–556 (1992).
28. Ramprasad, R. First principles study of oxygen vacancy defects in tantalum pentoxide. *J. Appl. Phys.* **94**, 5609–5612 (2003).
29. Pérez-Walton, S., Valencia-Balvín, C., Padilha, A. C. M., Dalpian, G. M. & Osorio-Guillén, J. M. A search for the ground state structure and the phase stability of tantalum pentoxide. *J. Phys. Condens. Matter* **28**, 035801 (2015).
30. Lee, S.-H., Kim, J., Kim, S.-J., Kim, S. & Park, G.-S. Hidden structural order in orthorhombic Ta_2O_5. *Phys. Rev. Lett.* **110**, 235502 (2013).
31. Terao, N. Structure des Oxides de Tantale. *Jpn. J. Appl. Phys.* **6**, 21 (1967).
32. Fukumoto, A. & Miwa, K. Prediction of hexagonal Ta_2O_5 structure by first-principles calculations. *Phys. Rev. B* **55**, 11155–11160 (1997).
33. Stephenson, N. C. & Roth, R. S. Structural systematics in the binary system Ta_2O_5–WO3. V. The structure of the low-temperature form of tantalum oxide L-Ta_2O_5. *Acta Crystallogr. B* **27**, 1037–1044 (1971).
34. Grey, I. E., Mumme, W. G. & Roth, R. S. The crystal chemistry of L-Ta_2O_5 and related structures. *J. Solid State Chem.* **178**, 3308–3314 (2005).
35. Aleshina, L. A. & Loginova, S. V. Rietveld analysis of X-ray diffraction pattern from β-Ta_2O_5 oxide. *Crystallogr. Rep.* **47**, 415–419 (2002).
36. Izumi, F. & Kodama, H. A new modification of tantalum(V) oxide. *J. Common Met.* **63**, 305–307 (1979).
37. Zibrov, I. P., Filonenko, V. P., Sundberg, M. & Werner, P.-E. Structures and phase transitions of B-Ta_2O_5 and Z-Ta_2O_5: Two high-pressure forms of Ta_2O_5. *Acta Crystallogr. B* **56**, 659–665 (2000).
38. Askeljung, C., Marinder, B.-O. & Sundberg, M. Effect of heat treatment on the structure of L-Ta_2O_5: A study by XRPD and HRTEM methods. *J. Solid State Chem.* **176**, 250–258 (2003).
39. Lagergren, S. *et al.* On the tantalum–oxygen system. *Acta Chem. Scand.* **6**, 444–446 (1952).
40. Farhan, M. S., Zalnezhad, E. & Bushroa, A. R. Properties of Ta_2O_5 thin films prepared by ion-assisted deposition. *Mater. Res. Bull.* **48**, 4206–4209 (2013).
41. He, X. *et al.* Reversible resistance switching properties in Ti-doped polycrystalline Ta_2O_5 thin films. *Appl. Phys. A* **108**, 177–183 (2012).
42. Wang, K., Wu, H., Wang, X., Li, X. & Qian, H. Study of doping effects on Ta_2O_5–x/ TaOy based bilayer RRAM devices. In *2014 IEEE International Conference on Electron Devices and Solid-State Circuits* 1–2 (2014). https://doi.org/10.1109/EDSSC.2014.7061254.
43. Kukli, K. *et al.* Atomic layer deposition and properties of mixed Ta_2O_5 and ZrO_2 films. *AIP Adv.* **7**, 025001 (2017).

44. Hafner, J. & Kresse, G. The Vienna AB-initio simulation program VASP: An efficient and versatile tool for studying the structural, dynamic, and electronic properties of materials. In *Properties of Complex Inorganic Solids* (eds Gonis, A. *et al.*) 69–82 (Springer US, 1997). https://doi.org/10.1007/978-1-4615-5943-6_10.
45. Kresse, G. & Furthmüller, J. Efficient iterative schemes for ab initio total-energy calculations using a plane-wave basis set. *Phys. Rev. B* **54**, 11169–11186 (1996).
46. Perdew, J. P. *et al.* Restoring the density-gradient expansion for exchange in solids and surfaces. *Phys. Rev. Lett.* **100**, 136406 (2008).
47. Scheidemantel, T. J., Ambrosch-Draxl, C., Thonhauser, T., Badding, J. V. & Sofo, J. O. Transport coefficients from first-principles calculations. *Phys. Rev. B* **68**, 125210 (2003).
48. Mahan, G. D. & Sofo, J. O. The best thermoelectric. *Proc. Natl. Acad. Sci.* **93**, 7436–7439 (1996).
49. Madsen, G. K. H. & Singh, D. J. BoltzTraP. A code for calculating band-structure dependent quantities. *Comput. Phys. Commun.* **175**, 67–71 (2006).
50. Andreoni, W. & Pignedoli, C. A. Ta_2O_5 polymorphs: Structural motifs and dielectric constant from first principles. *Appl. Phys. Lett.* **96**, 062901 (2010).
51. Sahu, B. R. & Kleinman, L. Theoretical study of structural and electronic properties of $\beta-Ta_2O_5$ and $\delta-Ta_2O_5$. *Phys. Rev. B* **69**, 165202 (2004).
52. Nashed, R., Hassan, W. M. I., Ismail, Y. & Allam, N. K. Unravelling the interplay of crystal structure and electronic band structure of tantalum oxide (Ta_2O_5). *Phys. Chem. Chem. Phys.* **15**, 1352–1357 (2013).
53. Wu, Y.-N., Li, L. & Cheng, H.-P. First-principles studies of Ta_2O_5 polymorphs. *Phys. Rev. B* **83**, 144105 (2011).
54. Wu, X. M., Soss, S. R., Rymaszewski, E. J. & Lu, T.-M. Dielectric constant dependence of Poole-Frenkel potential in tantalum oxide thin films. *Mater. Chem. Phys.* **38**, 297–300 (1994).
55. Chun, W.-J. *et al.* Conduction and valence band positions of Ta_2O_5, TaON, and Ta_3N_5 by UPS and electrochemical methods. *J. Phys. Chem. B* **107**, 1798–1803 (2003).
56. Chaneliere, C., Autran, J. L., Devine, R. A. B. & Balland, B. Tantalum pentoxide (Ta_2O_5) thin films for advanced dielectric applications. *Mater. Sci. Eng. R Rep.* **22**, 269–322 (1998).
57. Knausenberger, W. H. & Tauber, R. N. Selected properties of pyrolytic Ta_2O_5 films. *J. Electrochem. Soc.* **120**, 927 (1973).
58. Cui, Z.-H. & Jiang, H. Theoretical investigation of Ta_2O_5, TaON, and Ta_3N_5: Electronic band structures and absolute band edges. *J. Phys. Chem. C* **121**, 3241–3251 (2017).
59. Fleming, R. M. *et al.* Defect dominated charge transport in amorphous Ta_2O_5 thin films. *J. Appl. Phys.* **88**, 850–862 (2000).
60. Hur, J.-H. First principles study of the strain effect on band gap of λ phase Ta_2O_5. *Comput. Mater. Sci.* **164**, 17–21 (2019).
61. Seki, S., Unagami, T., Kogure, O. & Tsujiyama, B. Formation of high-quality, magnetron-sputtered Ta_2O_5 films by controlling the transition region at the Ta_2O_5/Si interface. *J. Vac. Sci. Technol. A* **5**, 1771–1774 (1987).
62. Mehra, R. M., Jasmina, Mathur, P. C. & Taylor, P. C. Effect of sulfur doping on electrical conductivity of a-Si:H. *Thin Solid Films* **312**, 170–175 (1998).
63. Kumar, S., Kashyap, S. C. & Chopra, K. L. X-ray photoelectron spectroscopy studies of *n* -type bismuth-modified amorphous thin films of $Ge_{20}Se_{80}$ and As_2Se_3. *J. Appl. Phys.* **72**, 2066–2068 (1992).
64. Thompson, M. G. & Reinhard, D. K. Modification of amorphous hydrogenated silicon by co-sputtered aluminum. *J. Non-Cryst. Solids* **37**, 325–333 (1980).
65. Shkvarin, A. S. *et al.* Band gap width control by Cu intercalation into $ZrSe_2$. *J. Phys. Chem. C* **123**, 410–416 (2019).
66. But'ko, V. G., Gusev, A. A., Shevtsova, T. N. & Pashkevich, Yu. G. Changes of the electronic structure of a (8, 0) zigzag nanotube due to doping with potassium. *Low Temp. Phys.* **35**, 137–140 (2009).
67. Zhao, L., Clima, S., Magyari-Köpe, B., Jurczak, M. & Nishi, Y. Ab initio modeling of oxygen-vacancy formation in doped-HfOx RRAM: Effects of oxide phases, stoichiometry, and dopant concentrations. *Appl. Phys. Lett.* **107**, 013504 (2015).
68. Shi, Y. *et al.* First principle study of tritium trapping at oxygen vacancies in Li4SiO4. *J. Nucl. Mater.* **508**, 257–264 (2018).
69. Guo, Y. & Robertson, J. Comparison of oxygen vacancy defects in crystalline and amorphous Ta_2O_5. *Microelectron. Eng.* **147**, 254–259 (2015).
70. Zhang, F., Yang, C., Su, Y. & Wang, D. Carrier capture and emission properties of silicon interstitial defects in near SiC/SiO_2 interface region. *Appl. Surf. Sci.* **514**, 145889 (2020).
71. Cheng, X. *et al.* Effect of oxygen vacancy on the band gap and nanosecond laser-induced damage threshold of Ta_2O_5 films. *Chin. Phys. Lett.* **29**, 084207 (2012).
72. Song, Y., Magyari-Kope, B., Lin, Y. & Nishi, Y. Improving the high resistance state retention degradation of Al-doped HfOx based on ab initio simulations. In *2017 IEEE International Memory Workshop (IMW)* 1–4 (2017). https://doi.org/10.1109/IMW.2017.7939089.
73. Frascaroli, J., Volpe, F. G., Brivio, S. & Spiga, S. Effect of Al doping on the retention behavior of HfO_2 resistive switching memories. *Microelectron. Eng.* **147**, 104–107 (2015).
74. Ho, C.-T. *et al.* Formation of Sol–Gel-derived TaOxNy photocatalysts. *Chem. Mater.* **23**, 4721–4725 (2011).
75. Bredow, T. *et al.* Structure and stability of TaON polymorphs. *Z. Für Anorg. Allg. Chem.* **632**, 1157–1162 (2006).
76. Chen, S. & Wang, L.-W. Intrinsic defects and electronic conductivity of TaON: First-principles insights. *Appl. Phys. Lett.* **99**, 222103 (2011).
77. Yashima, M., Lee, Y. & Domen, K. Crystal structure and electron density of tantalum oxynitride, a visible light responsive photocatalyst. *Chem. Mater.* **19**, 588–593 (2007).
78. Qiang, Z. Effects of interaction between defects on the uniformity of doping HfO_2-based RRAM: a first principle study. *J. Semicond.* **34**, 032001 (2013).
79. Nadimi, E. *et al.* Interaction of oxygen vacancies and lanthanum in Hf-based high-k dielectrics: An ab initio investigation. *J. Phys. Condens. Matter* **23**, 365502 (2011).
80. Zhang, H. *et al.* Effects of ionic doping on the behaviors of oxygen vacancies in HfO_2 and ZrO2: A first principles study. In *2009 International Conference on Simulation of Semiconductor Processes and Devices* 1–4 (2009). https://doi.org/10.1109/SISPAD.2009.5290225.

Author contributions

M. S. I., S. G. and A.R. conceived the idea; J.L. designed this study, M. S. I. performed the simulations and prepared the draft of the manuscript. All authors discussed, analyzed the data, and contributed during the writing of the manuscript.

Competing interests

The authors declare no competing interests.

Additional information

Supplementary Information The online version contains supplementary material available at https://doi.org/10.1038/s41598-023-43888-z.

Correspondence and requests for materials should be addressed to M.S.I. or A.K.R.

Reprints and permissions information is available at www.nature.com/reprints.

Publisher's note Springer Nature remains neutral with regard to jurisdictional claims in published maps and institutional affiliations.

Open Access This article is licensed under a Creative Commons Attribution 4.0 International License, which permits use, sharing, adaptation, distribution and reproduction in any medium or format, as long as you give appropriate credit to the original author(s) and the source, provide a link to the Creative Commons licence, and indicate if changes were made. The images or other third party material in this article are included in the article's Creative Commons licence, unless indicated otherwise in a credit line to the material. If material is not included in the article's Creative Commons licence and your intended use is not permitted by statutory regulation or exceeds the permitted use, you will need to obtain permission directly from the copyright holder. To view a copy of this licence, visit http://creativecommons.org/licenses/by/4.0/.

© The Author(s) 2023